




Nanoarchitectonics of hierarchical PbS material for all-solid-state asymmetric supercapacitor

T. S. Bhat^{1,2} , A. V. Shinde³, A. A. Alat¹, and P. S. Patil^{1,*}

¹Thin Film Materials Laboratory, Department of Physics, Shivaji University, Kolhapur 416 004, Maharashtra, India

²School of Nanoscience and Biotechnology, Shivaji University, Kolhapur 416 004, India

³Department of Physics, Vivekanand College, Kolhapur 416004, Maharashtra, India

Received: 22 September 2021

Accepted: 1 March 2022

Published online:
22 March 2022

© The Author(s), under exclusive licence to Springer Science+Business Media, LLC, part of Springer Nature 2022

ABSTRACT

Present article reports morphology controlled synthesis of lead sulfide (PbS) thin films using cost-effective chemical method. The structural, morphological, and electrochemical studies of the samples were carried out. Rock-salt phase cubic structure formation is affirmed by XRD analysis. SEM micrograph describes the evolution of an exotic, anisotropic, 3D hierarchical dendritic architecture into microflowers as a function of reaction time. The optimized sample shows specific capacitance of 360 F g^{-1} at a scan rate of 5 mV s^{-1} . The all-solid-state asymmetric PbS//MnO₂ supercapacitor device shows cycling stability of 71% over 1000 cycles highlights the significance of hierarchical PbS nanostructures in supercapacitors.

1 Introduction

Supercapacitors have gained considerable attention in the electrochemical storage field due to their rapid charge/discharge rates, environmentally friendliness, high power density as well as long life cycle [1, 2]. Supercapacitive performance is mainly dependent on high surface area of electrode material along with the ease of transportation of ions between electrolyte and electroactive material [3]. Nowadays, it is highly required to engineer a new-class of electrode materials for supercapacitor application with higher energy as well as power density [4].

Recently, various metal chalcogenides have been recognized as a promising candidate for supercapacitor electrode material due to their high theoretical capacities, excellent conductivity, and accessible oxidation states [5–14]. Among these, Lead sulfide (PbS) is an important—semiconductor material with a near-infrared direct low bandgap (0.41 eV at 300 K) and a high exciton Bohr radius (18 nm), which is advantageous for electron transport [15–18]. Furthermore, PbS is less difficult to produce [19]. Based on these benefits PbS has an intriguing possibility for its use as an electrode material in pseudocapacitors [20, 21].

T. S. Bhat and A. V. Shinde have contributed equally to this work.

Address correspondence to E-mail: psp_phy@unishivaji.ac.in

It is observed that morphological control is frequently used in manufacturing the materials to improve the performance of energy storage devices particularly in cycle stability and rate capability [22, 23]. Microstructures increase the mechanical strength of active materials, preventing aggregation and structural collapse, which improves cycle stability. Nanostructures, on the other hand, enhance the electroactive regions of the active materials, ensuring high performance and rate capability. Nonetheless, hierarchical systems have several problems in precise control and low-cost preparation [20].

In recent years hierarchical nanostructured lead chalcogenides are used in many disciplines, such as nonlinear optical switches [24], energy storage devices [25], solar cell sensitizers [26, 27], and optoelectronic devices [28]. Particularly, PbS finds use in sensors, solar cells, infrared radiations, phototransistors, lasers, optoelectronic devices, and thermoelectric devices due to its unique size and shape-dependent characteristics [29–35].

In the present work, PbS thin films are prepared using facile, cost-effective hydrothermal and screen print method. Various characterization techniques were used to investigate the structural, morphological, and electrochemical characteristics of PbS thin films. The growth mechanism of hierarchical PbS microstructures was investigated. The optimized PbS thin film sample is used to fabricate and analyzed the performance of all-solid-state asymmetric PbS//MnO₂ supercapacitor device.

2 Experimental details

2.1 Materials

All the analytical grade chemicals were purchased from Sigma Aldrich and used without further purification.

2.2 Synthesis of PbS nanostructures

In actual synthesis of PbS thin films, 0.1 M aqueous solution of lead nitrate in 10 ml of double distilled water (DDW), added into 0.5 M thiourea in 10 ml of DDW. After stirring for 10 min, this mixture is poured into the 25 ml teflon-lined stainless steel autoclave. This system is then kept into the muffle furnace at 100 °C for 1 h. Then the system is allowed

to cool down to room temperature. The same reaction was carried out at 2 and 3 h. The obtained black precipitate was denoted as PbS: H1, PbS: H2, and PbS: H3 obtained at the reaction time 1 h, 2 h, and 3 h, respectively. The precipitate was washed several times with ethanol and DDW and dried in oven at 60 °C for 1 h. Figure 1A shows PbS powder obtained by hydrothermal method along with synthesis parameters.

2.3 PbS electrode preparation

Electrodes of PbS have been fabricated by depositing these active materials on flexible stainless steel substrates by screen print method. In typical route, the working electrodes were prepared by mixing the as-prepared active material, i.e., PbS powder (80 wt.%), carbon black (10 wt.%) and polyvinylidene fluoride (PVDF) (10 wt.%) with small amounts of ethanol to obtain a uniform black paste. The homogeneous slurry of PbS has been coated on polished flexible stainless steel substrate with active area of 1 cm² and dried at 80 °C in a vacuum oven for 12 h. The three electrodes PbS: H1, PbS: H2, and PbS: H3 formed were used for further characterizations.

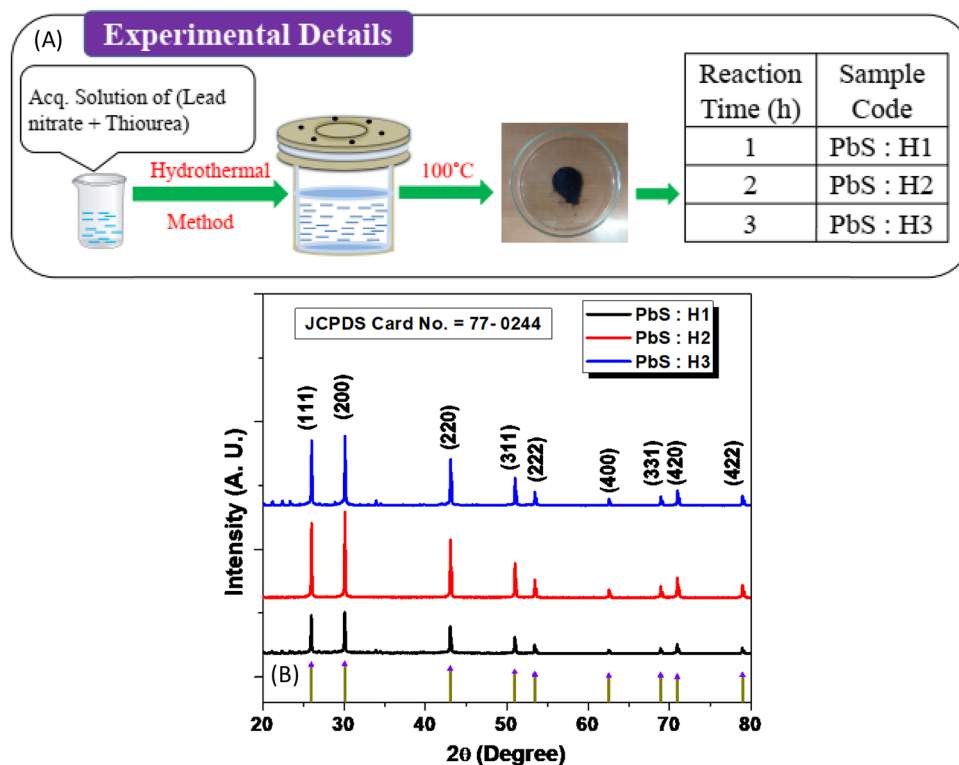
2.4 Synthesis of MnO₂ thin film

Here, MnO₂ thin film was used as cathode. It is prepared by simple CBD method. The precursor solution consist of 0.5 M KMnO₄ in 50 ml solution. The solution was stirred for 15 min. at room temperature, subsequently 0.5 M HCl is added into the solution. A well cleaned flexible stainless steel substrate is dipped into the solution for 6 h at 60 °C to get uniform thin film of MnO₂.

2.5 Preparation of CMC-Na₂SO₄ gel electrolyte

In a typical preparation, 2 g carboxymethyl cellulose (CMC) was dissolved in 30 ml of DDW under constant magnetic stirring. After CMC was completely dissolved, 2 g Na₂SO₄ was added into CMC solution and the resulting mixture was vigorously stirred at 70 °C till the formation of transparent, viscous, and homogeneous solution. This viscous solution was used as a gel electrolyte for the fabrication of asymmetric supercapacitors.

Fig. 1 **A** Schematic representation of PbS powder formation via hydrothermal method. **B** X-ray diffraction patterns of PbS samples. Vertical lines show the standard JCPDS peaks



2.6 Characterization of PbS thin films

The XRD pattern of the films was recorded using X-ray powder diffractometer (Bruker AXS Analytical Instruments Pvt. Ltd., Germany, Model: D2 phaser). Surface morphology was examined using SEM (JEOL JSM-6360). The deposited mass on the substrate was calculated by using weight difference method. The specific surface area of a material was calculated by Brunauer, Emmett and Teller (BET) model Quantachrome Instruments v45.02. The electrochemical characterizations were carried out by using automatic battery cyclor unit (WBCS3000) while electrochemical impedance studies were carried out using AUTOLAB PGSTAT100 FRA 32 potentiostat.

3 Results and discussion

3.1 X-ray diffraction (XRD)

The XRD pattern for the PbS thin film samples is shown in Fig. 1B. The appearance of diffraction peaks at 30.2°, 25.9°, and 43.1° corresponds to the (200), (111), and (220) hkl planes, respectively, indicating the predominant growth of crystallites along the [100] direction. Other weak peaks (311), (222), (400), (331),

(420), and (422) correspond to the rock-salt phase (FCC) cubic structure of PbS (JCPDS: 77-0244). The sharp and strong diffraction peaks demonstrate the product's excellent crystallization. The XRD pattern revealed no impurity phases, confirming the excellent purity of the PbS samples. The crystallite size was estimated from the basic Scherrer equation [36],

$$D = \frac{K\lambda}{\beta \cos \theta}, \quad (1)$$

where D is the average crystallite size, λ is the x-ray wavelength, β is the width of the x-ray peak on the 2θ axis, normally measured as full width at half maximum (FWHM), θ is the Bragg angle, and K is the so-called Scherrer constant. K depends on the crystallite shape and the size distribution, indices of the diffraction line. The average crystallite size calculated from Scherrer formula, was found to be ~ 73, 85, 94 nm for PbS: H1, PbS: H2, and PbS: H3 samples, respectively [37, 38].

3.2 Scanning electron microscopy (SEM)

SEM images of PbS samples are shown in Fig. 2A. These images depict the formation of hierarchical nanostructures of lead sulfide. Sample PbS: H1 shows the fern like structures with ~ 4 μm arm length and

each arm has dendrite like structures which are ~ 800 nm in size. As the deposition time increased there is formation of micro-flowers along with fern like structures as seen in sample PbS: H2. The micro-flowers are made up of micro-petals with size ~ 1.5 μm , which enhance the specific surface area of the electrode (Fig. S1). The PbS formed at 3 h has fern like structures with obelisk shapes at the end of dendrite, which has a length of ~ 5 μm and diameter ~ 1.2 μm .

3.2.1 Growth mechanism

The reduction in surface energy is thought to be the major driving mechanism for simple particle development during the growth stage. The surface energy (γ) of an FCC structure is thought to be of the order $\gamma\{111\} < \gamma\{100\} < \gamma\{110\} < \gamma\{hkl\}$ where hkl denotes a high index facet [39, 40].

According to Bashouti and Lifshitz [41], the reaction temperature and time influence the relative thermodynamic or kinetic growth rate of crystals in various orientations. In general, the formation of lead chalcogenide crystals consists of two phases initial

nucleation and subsequent development [42, 43]. Because of their extremely symmetric cubic rock-salt crystal structures, the seeds form as polyhedra during nucleation, exposing six $\{100\}$ and eight $\{111\}$ facets. The surface energy determines the development rates on different facets throughout the growth stage. The variation in relative growth rates of the six $\{100\}$ faces and the eight $\{111\}$ faces of seeds with a truncated octahedron shape is widely assumed to be responsible for nanoscale geometries. The quicker development along the eight $\langle 111 \rangle$ directions perpendicular to $\{111\}$ faces leads in the removal of such faces and the production of $\{100\}$ faceted cubes (Fig. 2B). If perpendicular growth to $\{100\}$ faces is favored, such faces ultimately vanish, and the resultant morphologies are eight-faced octahedra with $\{111\}$ faces. If the latter development is significantly quicker than that along the $\langle 111 \rangle$ directions and longer growth durations are permitted, six-branched star-shaped PbS is produced as a result of the growth of the octahedral structures along the six $\langle 100 \rangle$ directions (Fig. 2B). However, if the quicker growth along the eight $\langle 111 \rangle$ directions is maintained,

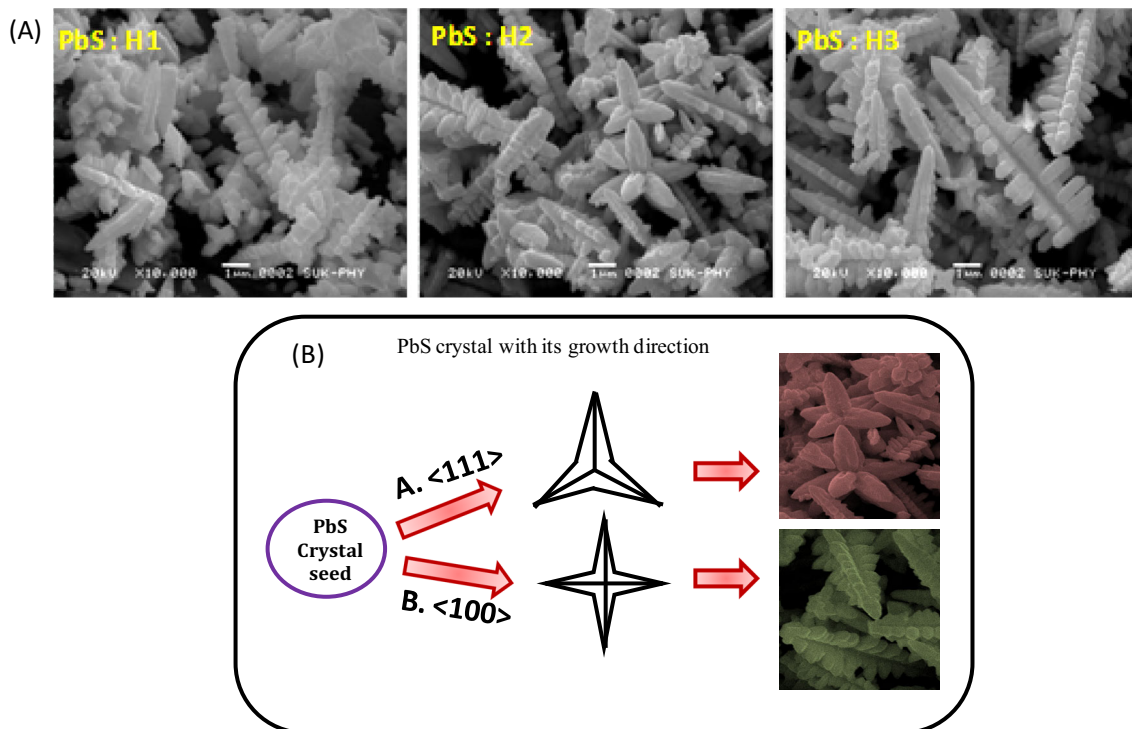


Fig. 2 **A** SEM images at $\times 10000$ magnification of PbS samples synthesized at 1 h, 2 h, and 3 h by hydrothermal route shows hierarchical nanostructures. **B** Growth mechanism shows

formation of hierarchical PbS nanostructures **A** one arm has three ridges and **B** one arm has four ridges

octapod formations emerge. Hierarchical PbS nanostructures are produced in this manner [44].

3.3 Electrochemical characterization of PbS thin films

3.3.1 Electrochemical measurements

The electrodes on flexible stainless steel substrate were cut into 1 cm² samples and then used as working electrodes. The electrochemical performances were measured in a three electrode system with 1 M Na₂SO₄ electrolyte using cyclic voltammetry (CV), galvanostatic charge–discharge (GCD), and EIS measurements. Platinum wire and an Ag/AgCl electrode were used as the counter and reference electrodes, respectively. The specific capacitance (*C*_{sp}) of the electrodes was calculated from CV and GCD measurements, using the following equations, respectively [45, 46]:

$$C_{sp} = \frac{1}{mv(V_c - V_a)} \int_{V_a}^{V_c} I(V)dV, \quad (2)$$

where, *C*_{sp} is the value of PbS electrode by CV study, can be computed by integrating the area under CV and then dividing by the scan rate (*v*), the mass of the deposited material (*m*) in the electrode and the potential window (*V*_a – *V*_c).

$$C_{sp} = \frac{I_d \times T_d}{\Delta V \times m}, \quad (3)$$

where, *C*_{sp} is specific capacitance, *I*_d is discharged current, *T*_d is the discharge time, ΔV is working potential window, and '*m*' is the mass of deposited material which is estimated through the following equation,

$$m = m_2 - m_1, \quad (4)$$

where, *m*₂ is the mass of the flexible stainless steel substrate with the electroactive material and *m*₁ is the mass of the flexible stainless steel substrate without the electroactive material.

As two different electrodes materials are used in fabrication of asymmetric device, the balancing of mass ratio from cathode to anode is done by following equation,

$$\frac{m^+}{m^-} = \frac{(C^- \times \Delta V^-)}{(C^+ \times \Delta V^+)}, \quad (5)$$

where, *m*⁺, *m*[–], *C*⁺, *C*[–], ΔV^+ , ΔV^- are the mass, specific capacitance, working potential window of

cathode and anode, respectively. Ragone plot is further used to relate energy densities (ED) and power densities (PD) to examine the performance of electrode. The ED and PD values were calculated by the following equations,

$$ED = \frac{0.5 \times C_s \times (V_{max}^2 - V_{min}^2)}{3.6}, \quad (6)$$

$$PD = \frac{E \times 3600}{T_d}. \quad (7)$$

The typical Cyclic Voltammetry (CV) curves measured at various scan rates in 1 M Na₂SO₄ electrolyte for PbS: H1, PbS: H2, PbS: H3 are shown in Fig. 3A, B, C, respectively. The area under the CV curves grows with scan rate for all three samples, indicating that the electrolyte ions use the active electrode material for all three electrodes. It is noticed that the PbS: H2 sample has a greater area under the curve with symmetric nature than the other two samples, indicating that it has better electrochemical performance than other two samples. The graph of specific capacitance as a function of scan rate for all samples is shown in Fig. 3D. As the scan rate changes from 5 to 100 mV s^{–1}, the specific capacitance of PbS: H1, PbS: H2, and PbS: H3 varies from 320 to 40, 360–270, and 210–40 F g^{–1}, respectively. Specific capacitance values are greater at low scan rates than at higher scan rates. This is owing to the fact that at lower scan rates, the maximal electroactive surface area accessible for electrochemical reaction is greater. Only the outside surface area is available for electrochemical reaction at higher scan rates [25]. At specific scan rate, specific capacitance of PbS: H2 sample is higher than other two samples. It is attributed as PbS: H2 sample has higher geometrical area at electrode surface which allows more insertion of ions than other two samples which allow to maximize the efficiency of electrochemical redox reactions [25].

Charge discharge experiments were carried out at various current densities to investigate the rate capabilities of as-prepared PbS thin films (0.25–1 mA cm^{–2}). Figure 4A–C depicts the charge–discharge behavior of PbS thin films at different current densities for three samples. Figure 4 shows the asymmetric behavior of the charge–discharge curve, indicating the pseudocapacitive behavior of all PbS samples [47]. The curve of specific capacitance as a function of current density is shown in Fig. 4D. Based on this graph, we can infer that the PbS: H2

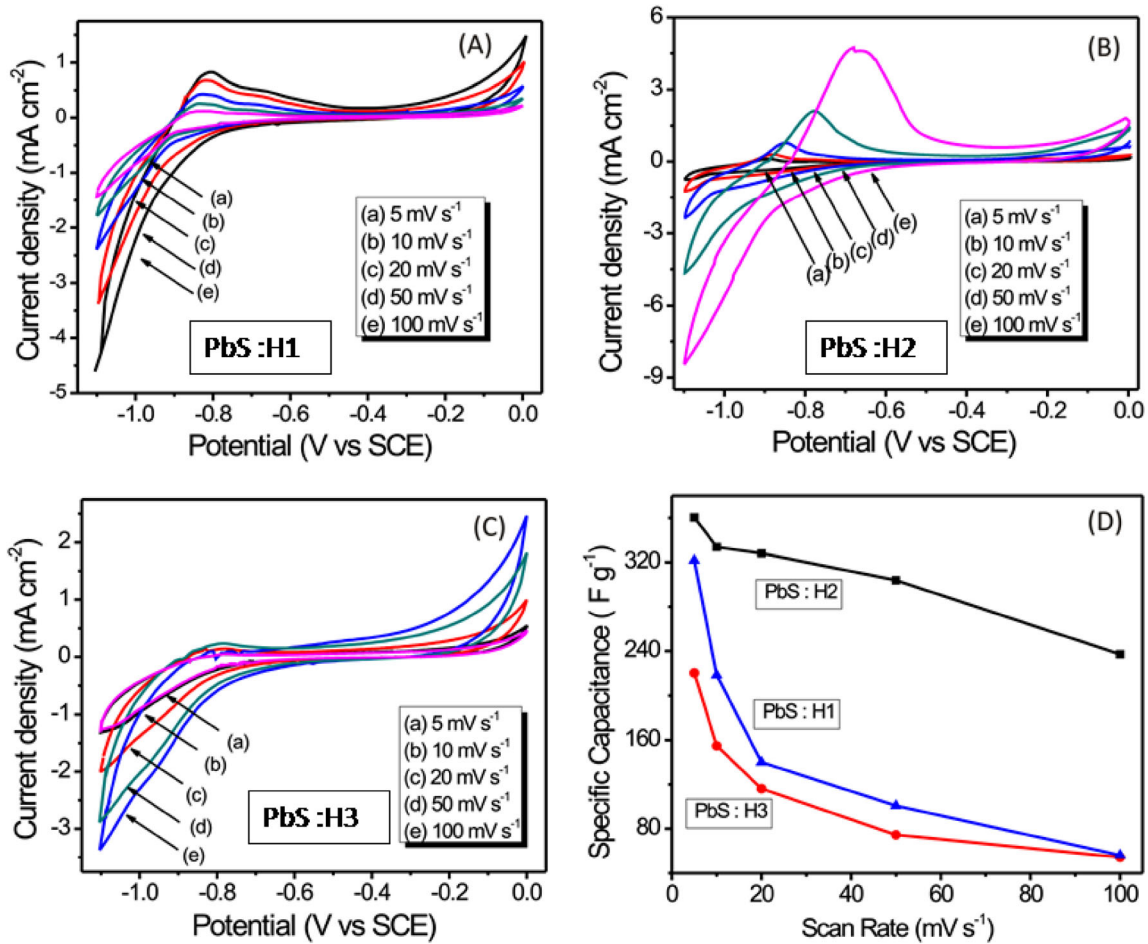


Fig. 3 CV curves of all PbS electrodes at scan rate 100 mV s^{-1} . The CV curves of **A** PbS: H1, **B** PbS: H2, **C** PbS: H3 at different scanning rates. **D** Variation of specific capacitance with different scanning rates of different PbS electrodes in 1 M Na_2SO_4 electrolyte

sample has a maximum specific capacitance of 360 Fg^{-1} at scan rate of 5 mV s^{-1} , which is significantly more than other two samples due to relatively higher surface area of PbS: H2 sample.

Impedance measurements were taken in order to study the electrochemical properties of the electrode and electrolyte in a quantitative manner. The electrochemical impedance of several PbS electrodes (PbS: H1, PbS: H2, PbS: H3) was measured across a frequency range of 100 mHz–100 MHz. Figure 5 depicts the Nyquist plots of all PbS electrodes. The semicircles in the high frequency range are seen in the Nyquist plots of PbS: H1, PbS: H2, and PbS: H3 thin films. PbS: H2 and PbS: H3 thin films have a longer tail in the low frequency region than PbS: H1 thin film. Table 1 summarizes the computed values of R_{ct} and R_s . Based on these results, it is inferred that the R_{ct} and R_s values for PbS: H2 thin film are lower than those for other samples. The EIS results were

strongly support to the CV and charge–discharge study.

3.4 Fabrication of all-solid-state asymmetric PbS// MnO_2 supercapacitor

PbS: H2 sample was utilized as anode in the fabrication of the asymmetric device, whereas MnO_2 thin film was used as cathode. The fundamental design of an asymmetric device consists of two electrodes and a separator that prevents direct contact between the electrodes while allowing ion transport between them. The Carboxymethyl cellulose (CMC)- Na_2SO_4 - gel electrolyte was pasted between two electrodes, and electrical connections were formed at the electrodes. To avoid direct contact, gel electrolyte pasted electrodes are wrapped with nonconductive bands. To eliminate loose packing and air gaps, the

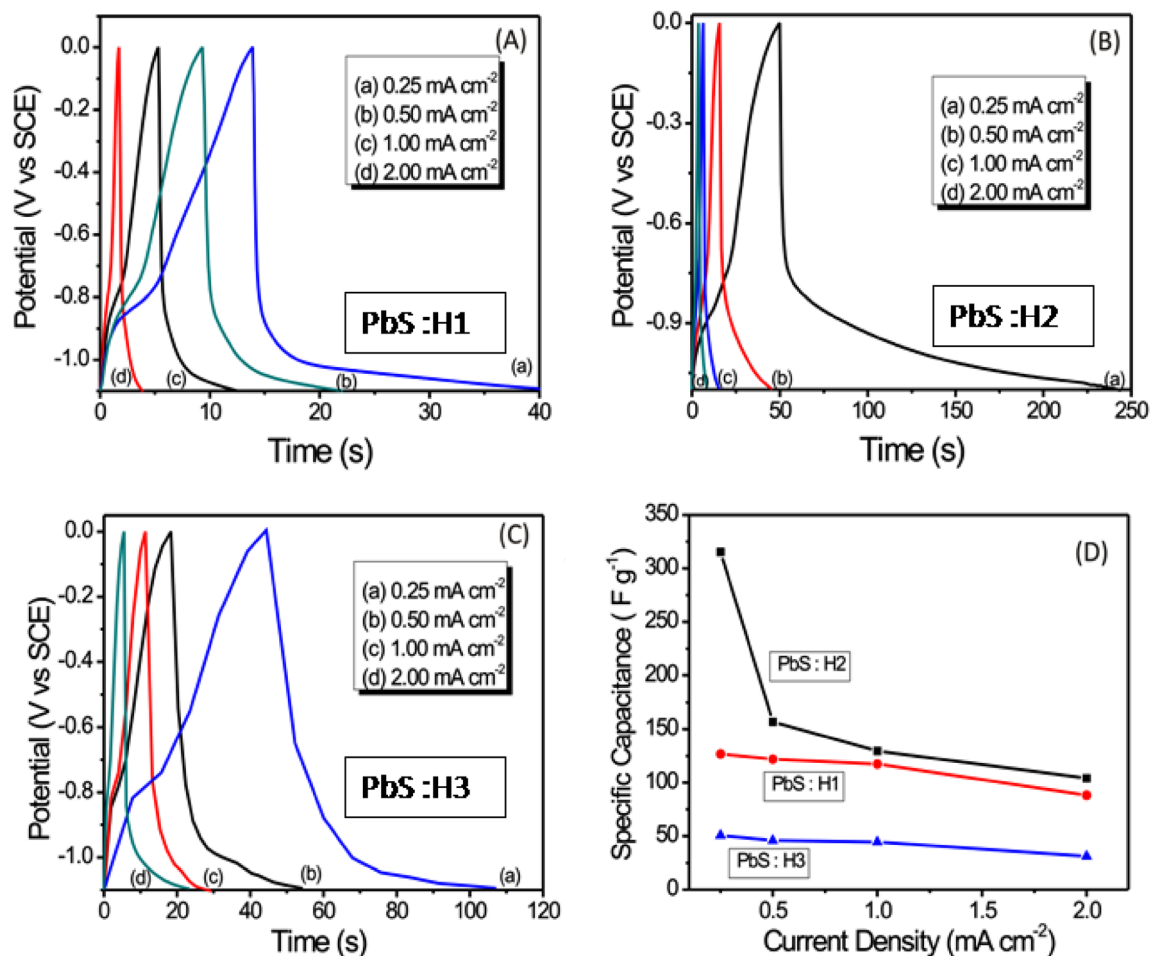


Fig. 4 Charge–discharge curves all PbS thin films electrodes **A** PbS: H1, **B** PbS: H2, **C** PbS: H3 in 1 M Na₂SO₄ electrolyte at different current densities. **D** Variation of specific capacitance at different current densities of different PbS electrodes in 1 M Na₂SO₄ electrolyte

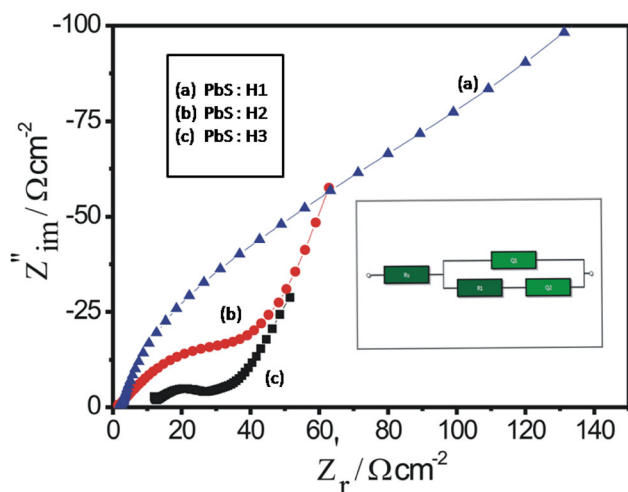


Fig. 5 Nyquist plot of all PbS thin film electrodes (PbS: H1, PbS: H2, PbS: H3) in 1 M Na₂SO₄ electrolyte

manufactured device is put up under 1 ton pressure for 15 min [48].

3.5 Electrochemical characterization of all-solid-state asymmetric PbS//MnO₂ supercapacitor

The electrochemical properties of an asymmetric supercapacitor device are investigated across an operating potential range of 0 – +0.65 V. The capacity to operate at a greater rate is desired for supercapacitor devices. The device's rate capability means that it can sustain electrochemical performance at both low and high scan rates or current densities. As a result, CVs were measured at different scan speeds ranging from 5 to 100 mV s⁻¹ to get an understanding of the rate capabilities of an asymmetric supercapacitor device (Fig. 6A). The device

Table 1 Electrochemical parameters of PbS thin films measured through EIS

Sample code	Specific capacitance ($F\ g^{-1}$) (at scan rate $5\ mV\ s^{-1}$) ($\pm 5\%$)	R_s ($\Omega\ cm^{-2}$) ($\pm 5\%$)	R_{ct} ($\Omega\ cm^{-2}$) ($\pm 5\%$)	Q_1 ($C\ cm^{-2}$) ($\pm 5\%$)	Q_2 ($C\ cm^{-2}$) ($\pm 5\%$)
PbS: H1	320	3.68	0.98	0.0598	0.0458
PbS: H2	360	2.52	0.32	0.0128	0.0113
PbS: H3	210	11.98	2.10	0.0987	0.0698

retains its CV form even at a high scan rate of $100\ mV\ s^{-1}$, and the increase in current density with scan rate suggests that the asymmetric supercapacitor device has a better capacitive characteristic [48, 49]. Figure 6B shows GCD curves for asymmetric device at different current densities at 0.5 – $1.5\ mA\ cm^{-2}$. The fact that the GCD curves are not fully symmetric demonstrates pseudocapacitive behavior, which is consistent with the findings of CV investigations. The early area of the discharge profile displays a relatively tiny potential drop due to electrode internal resistance or resistance produced at the electrical contact [50]. Figure 6C shows graph of specific capacitance versus scan rate of all-solid-state asymmetric PbS: H2//MnO₂ supercapacitor device. The maximum specific capacitance of $48\ F\ g^{-1}$ is obtained at scan rate of $5\ mV\ s^{-1}$ which is decreased to $22\ F\ g^{-1}$ at scan rate of $100\ mV\ s^{-1}$. The specific capacitance of $30\ F\ g^{-1}$ is obtained at current density of $0.5\ mA\ cm^{-2}$ (Fig. 6D). The specific capacitance derived from CV and GCD differs because the specific capacitance measured by CV is at a single potential, but the specific capacitance obtained from GCD is an average capacitance across a potential range of 0.0 – $+0.65\ V$. Averaging capacitances across a voltage range yields various specific capacitances [48–51]. When it comes to energy storage devices, the values of energy density and power density are crucial. These words define the practical use of an energy storage system. As a result, using the GCD curves, values of energy density and power density of an asymmetric device at different current densities are computed (Fig. 6E). The maximum energy density of $2.72\ Wh\ kg^{-1}$ and power density of $14\ kW\ kg^{-1}$ are obtained for all-solid-state asymmetric PbS: H2//MnO₂ supercapacitor.

Another critical aspect of determining the practical usefulness of an asymmetric device is its electrochemical cycle stability. As a result, the electrochemical stability was tested by repeating CV

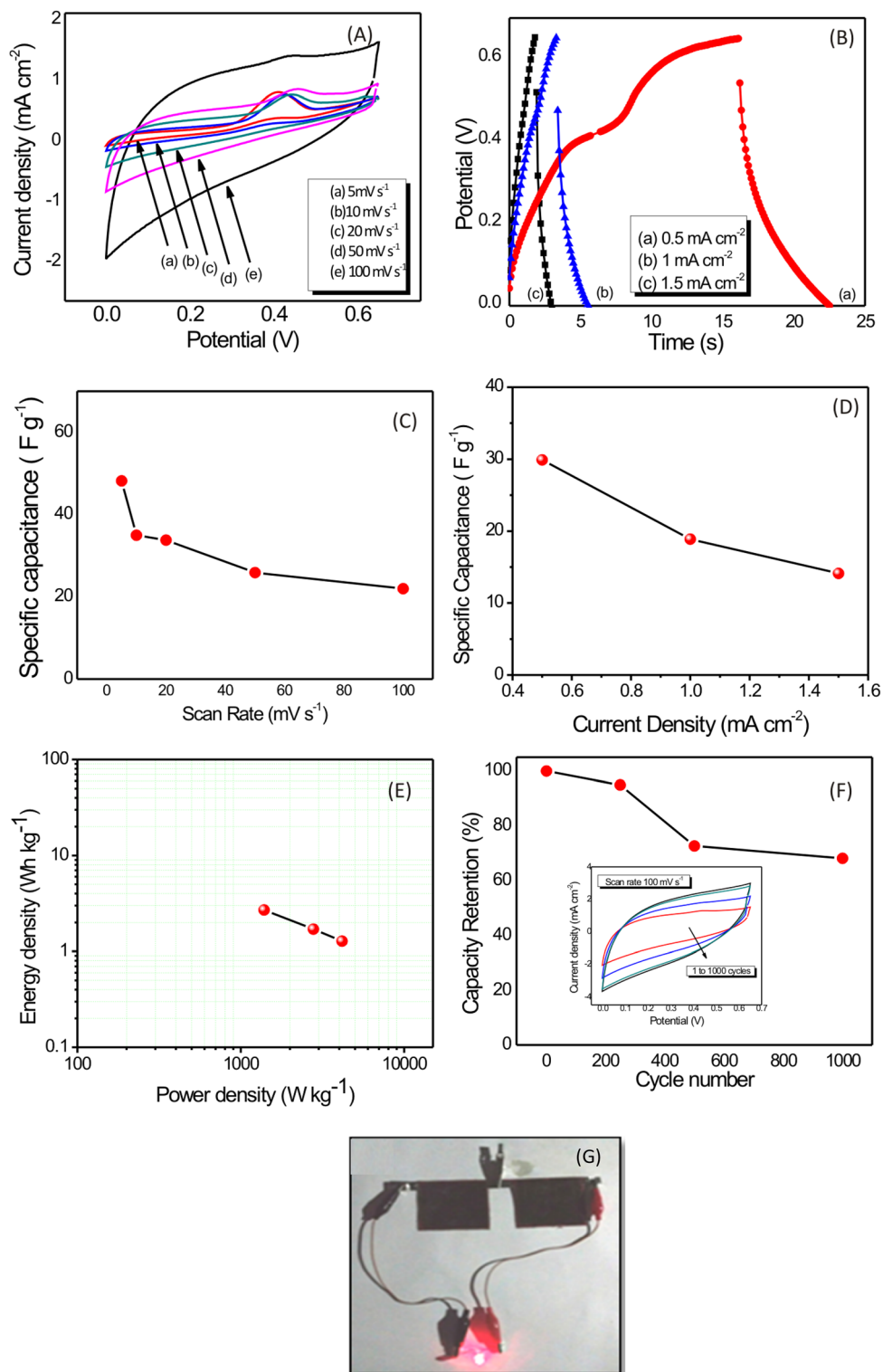
measurements for 1000 cycles at a scan rate of $100\ mV\ s^{-1}$. Figure 6F depicts a graph of capacity retention Vs CV cycle number, demonstrating 71% capacity retention over 1000 CV cycles. A red light emitting diode (LED) is blazed to demonstrate the practical usability of an asymmetric supercapacitor device. Figure 6G shows two all-solid-state asymmetric PbS: H2//MnO₂ supercapacitor devices linked in series for 30 s; lights up single LED for up to 1 min demonstrating the commercial viability of the device.

4 Conclusion

In conclusion, PbS thin films were deposited on flexible stainless steel substrate using a simple and cost-effective chemical process, and their supercapacitor performance was evaluated. The rock-salt phase cubic structure of PbS is confirmed by XRD. The growth of an unusual, anisotropic 3D hierarchical dendritic architecture into microflowers takes place as a function of reaction time and it is shown by SEM images. The growth mechanism of hierarchical PbS nanostructures is investigated. Because of its extremely symmetric cubic rock-salt crystal structure, the seed crystallizes as polyhedra during nucleation and growth, exposing six {100} and eight {111} facets. The rapid development along the {111} plane results in the production of PbS cubes, whereas the slow growth along the {100} plane results in the progressive transition of the PbS cubes to microcrystals with branching multiple arms. The enhanced surface area of hierarchical PbS nanostructures is helpful in energy storage devices.

At a scan rate of $5\ mV\ s^{-1}$, the PbS:H2 sample has a maximum specific capacitance of $360\ F\ g^{-1}$. In addition, all-solid-state asymmetric PbS//MnO₂ supercapacitor device shows maximum specific capacitance of $48\ F\ g^{-1}$ at a scan rate of $5\ mV\ s^{-1}$, coupled with maximum energy density and power

Fig. 6 **A** CV curves at various scan rates, **B** CD curves at various current densities, **C** Graph of specific capacitance versus scan rate, **D** Graph of specific capacitance versus current densities, **E** Ragone plot, **F** Graph of capacity retention at various cycle numbers for all-solid-state asymmetric PbS: H₂/MnO₂ supercapacitor device **G** Single LED glows upto 1 min by connecting two all-solid-state asymmetric PbS: H₂/MnO₂ supercapacitor devices in series combination (Charged upto 30 s)



density of 2.72 Wh kg⁻¹ and 14 kW kg⁻¹, respectively. Furthermore, after 1000 CV cycles, the supercapacitor device exhibits cycling stability of 71% concludes that, PbS thin films have the potential to be used in supercapacitors.

Acknowledgements

All the authors are thankful to Physics Instrumentation Facility Centre (PIFC), Department of Physics,

Shivaji University, Kolhapur for providing sample characterization facilities.

Author contributions

Conceptualization: TSB. Methodology: AAA. Formal analysis and investigation: TSB, AVS. Writing—original draft preparation: TSB. Writing—review and editing: TSB, AVS. Funding acquisition: PSP. Resources: PSP. Supervision: PSP.

Funding

The authors have not disclosed any funding.

Data availability

All data generated or analyzed during this study are included in this published article (and its supplementary information files).

Declarations

Conflict of interest There is no conflict of interest.

Supplementary Information: The online version contains supplementary material available at <http://doi.org/10.1007/s10854-022-08024-z>.

References

- P. Simon, Y. Gogotsi, B. Dunn, *Science* **343**, 1210 (2014)
- Y. Shao, J. Li, Y. Li, H. Wang, Q. Zhang, R.B. Kaner, *Mater. Horiz.* **4**, 1145 (2017)
- P. Simon, Y.Y. GoGotSi, *Nat. Mater.* **7**, 845 (2008)
- Y. Gogotsi, P. Simon, *Science* **334**, 917 (2011)
- S.A. Pawar, D.S. Patil, J.C. Shin, *Mater. Today Chem.* **4**, 164 (2017)
- D.S. Patil, S.A. Pawar, J.C. Shin, *J. Alloys Compd.* **768**, 1076 (2018)
- S.A. Pawar, D.S. Patil, J.C. Shin, *Electrochim. Acta* **259**, 664 (2018)
- D.P. Dubal, N.R. Chodankar, D.H. Kim, P.G. Romero, *Chem. Soc. Rev.* **47**, 2065 (2018)
- D.S. Patil, S.A. Pawar, J.C. Shin, *Chem. Eng. J.* **335**, 693 (2018)
- A. Arulraj, N. Ilayaraja, V. Rajeshkumar, M. Ramesh, *Sci. Rep.* **9**, 10108 (2019)
- H.Y. Li, J.K. Feng, L. Xiang, J. Huang, B. Xie, J. Power Sources **457**, 228031 (2020)
- L. Naderi, S. Shahrokhian, *Chem. Eng. J.* **392**, 124880 (2020)
- N.R. Chodankar, A.K. Nanjundan, D. Losic, D.P. Dubal, J.B. Baek, *Mater. Today Adv.* **6**, 100053 (2020)
- S. Subhadarshini, E. Pavitra, G.S.R. Raju, N.R. Chodankar, D.K. Goswami, Y.K. Han, Y.S. Huh, N.C. Das, *A.C.S. Appl. Mater. Interfaces* **12**, 29302 (2020)
- J.L. Machol, F.W. Wise, R.C. Patel, D.B. Tanner, *Phys. Rev. B* **48**, 2819 (1993)
- X.F. Shen, X.P. Yan, *J. Mater. Chem.* **18**, 4631 (2008)
- B. Ding, M. Shi, F. Chen, R. Zhou, M. Deng, M. Wang, H. Chen, *J. Cryst. Growth.* **311**, 1533 (2009)
- A.J. Wang, Q.C. Liao, J.J. Feng, P.P. Zhang, Z.M. Zhang, J.R. Chen, *Cryst. Growth Des.* **12**, 832 (2012)
- Y. Wen, Q. Wang, L. Yin, Q. Liu, F. Wang, F. Wang, Z. Wang, K. Liu, K. Xu, Y. Huang, T.A. Shifa, C. Jiang, J. Xiong, J. He, *Adv. Mater.* **28**, 8051 (2016)
- B. Pandit, G.K. Sharma, B.R. Sankapal, *J. Colloid Interf. Sci.* **505**, 1011 (2017)
- Y. Dai, C. Wang, C. Zhang, H. Huang, S. Huang, P. Zuo, R. Xia, Y. Gao, X. Meng, *J. Alloys Compd.* **805**, 631 (2019)
- K. Qiu, Y. Lu, D. Zhang, J. Cheng, H. Yan, J. Xu, X. Liu, J. Kim, Y. Luo, *Nano Energy* **11**, 687 (2015)
- S.S. Patil, T.S. Bhat, A.M. Teli, S.A. Beknalkar, S.B. Dhavale, M.M. Faras, M.M. Karanjkar, P.S. Patil, *Engineered Science* **12**, 38 (2020)
- T.S. Bhat, A.S. Kalekar, D.S. Dalavi, C.C. Revadekar, A.C. Khot, T.D. Dongale, P.S. Patil, *J. Mater. Sci.* **30**, 17725 (2019)
- T.S. Bhat, A.V. Shinde, R.S. Devan, A.M. Teli, Y.R. Ma, J.H. Kim, P.S. Patil, *Appl. Phys. A* **124**, 34 (2018)
- T.S. Bhat, S.S. Mali, A.D. Sheikh, S.D. Korade, K.K. Pawar, C.K. Hong, J.H. Kim, P.S. Patil, *Opt. Mater.* **73**, 781 (2017)
- T.S. Bhat, S.S. Mali, A.D. Sheikh, N.L. Tarwal, S.D. Korade, C.K. Hong, J.H. Kim, P.S. Patil, *Mater. Today Comm.* **16**, 186 (2018)
- T.S. Bhat, S.A. Vanalakar, R.S. Devan, S.S. Mali, S.A. Pawar, Y.R. Ma, C.K. Hong, J.H. Kim, P.S. Patil, *J Mater Sci: Mater Electron.* **27**, 4996 (2016)
- D.B. Kuang, A.W. Xu, Y.P. Fang, H.Q. Liu, C. Frommen, D. Fenske, *Adv. Mater.* **15**, 1747 (2003)
- D.B. Wang, D.B. Yu, M.W. Shao, X.M. Liu, W.C. Yu, Y.T. Qian, *J. Cryst. Growth* **257**, 384 (2003)
- W.P. Lim, H.Y. Low, W.S. Chin, *J. Phys. Chem. B* **108**, 13093 (2004)
- S.A. McDonald, G. Konstantatos, S. Zhang, P.W. Cyr, E.J.D. Klem, L. Levina, E.H. Sargent, *Nat. Mater.* **4**, 138 (2005)
- K.R. Choudhury, Y. Sahoo, S. Jang, P.N. Prasad, *Adv. Funct. Mater.* **15**, 751 (2005)

34. Z.H. Zhang, S.H. Lee, J.J. Vittal, W.S. Chin, *J. Phys. Chem. B* **110**, 6649 (2006)
35. H. Zhang, M. Zuo, S. Tan, G.P. Li, S.Y. Zhang, *Nanotechnology* **17**, 2931 (2006)
36. B. D. Cullity, *Elements of X-RAY Diffraction*, Second Edition, Addison-Wesley Publishing Company INC, 1978.
37. S.K. Abdel-Aal, A.S. Abdel-Rahman, *J. Nanopart. Res.* **22**, 267 (2020)
38. S.K. Abdel-Aal, M.F. Kandeel, A.F. El-Sherif, A.S. Abdel-Rahman, *Phys. Status Solidi A* **218**, 2100036 (2021)
39. Z. Wang, *J. Phys. Chem. B* **104**, 1153 (2000)
40. Y. Xiong, Y. Xia, *Adv. Mater.* **19**, 3385 (2003)
41. M. Bashouti, E. Lifshitz, *Inorg. Chem.* **47**, 678 (2008)
42. T. Mokari, M.J. Zhang, P.D. Yang, *J. Am. Chem. Soc.* **129**, 9864 (2007)
43. T.J. Zhu, X. Chen, Y.Q. Cao, X.B. Zhao, *J. Phys. Chem. C* **113**, 8085 (2009)
44. M. Mohammadikish, F. Davar, M.R. Loghman-Estarki, *J. Mater. Sci.* **26**, 2937 (2015)
45. K.H. Oh, G.S. Gund, H.S. Park, *J. Mater. Chem. A* **6**, 22106 (2018)
46. A.A. Yadav, Y.M. Hunge, S. Liu, S.B. Kulkarni, *Ultrason Sonochem.* **56**, 290 (2019)
47. N. Chodankar, D. Dubal, G. Gund, C. Lokhande, *Electrochim Acta* **165**, 338 (2015)
48. N. Chodankar, G. Gund, D. Dubal, C. Lokhande, *RSC Adv.* **4**, 61503 (2014)
49. A.V. Shinde, N.R. Chodankar, V.C. Lokhande, A.C. Lokhande, T. Ji, J.H. Kim, C.D. Lokhande, *RSC Adv.* **6**, 58839 (2016)
50. Z. Fan, J. Yan, T. Wei, L. Zhi, G. Ning, T. Li, F. Wei, *Adv. Funct. Mater.* **21**, 2366 (2011)
51. H. Zhang, X. Zhang, H. Lin, K. Wang, X. Sun, N. Xu, C. Li, Y. Ma, *Electrochim Acta* **156**, 70 (2015)

Publisher's Note Springer Nature remains neutral with regard to jurisdictional claims in published maps and institutional affiliations.